Feller, K. D., Wilby, D., Jacucci, G., Vignolini, S., Mantell, J., Wardill, T. J., Cronin, T. W., & Roberts, N. W. (2019). Long-Wavelength Reflecting Filters Found in the Larval Retinas of One Mantis Shrimp Family (Nannosquillidae). *Current Biology*, *29*(18), 3101-3108. https://doi.org/10.1016/j.cub.2019.07.070

Title

Long-wavelength reflecting filters found in the larval retinas of one mantis shrimp family (Nannosquillidae)

Authors

Kathryn D. Feller[1†,2,3*], David Wilby[3,4†], Gianni Jacucci[5], Silvia Vignolini[5], Judith Mantell[6], Trevor J. Wardill[1†,2], Thomas W. Cronin[7], Nicholas W. Roberts[3]

Affiliations

[1] Ecology, Evolution and Behavior Department, 1479 Gortner Avenue, University of Minnesota, St. Paul, Minnesota, 55108, USA

[2] Physiology Development and Neuroscience Department, Physiological Laboratories, Downing Street, University of Cambridge, Cambridge, CB2 3EG, UK.

[3] School of Biological Sciences, University of Bristol, Bristol, BS8 1TQ, UK.

[4] Department of Biology, Lund University, Lund, 223 62, Sweden.

[5] Department of Chemistry, University of Cambridge, Cambridge, CB2 1EW, UK.

[6] Wolfson Bioimaging Facility, University of Bristol, Bristol, UK, BS8 1TD, UK.

[7] Department of Biological Sciences, 1000 Hilltop Circle, Baltimore, University of Maryland Baltimore County, Maryland, 21250, USA.

*Correspondence to: kate.feller@gmail.com

† present address

Summary

Animals are known to exploit either transmissive coloured filters or reflectors for adaptive visual benefits. Here we describe a new category of biological optical filter that acts simultaneously as both a transmissive spectral filter and narrowband reflector. Discovered in the larval eyes of only one family of stomatopod crustaceans (Nannosquillidae), each crystalline structure bisects the photoreceptive rhabdom into two tiers and contains an ordered array of membrane-bound vesicles with sub-wavelength diameters of 153 ± 5 nm. Axial illumination of these intrarhabdomal structures *in vivo* produces a narrow-band of yellow reflectance (mean peak reflectivity at 572 ± 18 nm). While analogous visual structures are not known in nature, the optical performance of these intrarhabdomal structural reflectors is similar to synthetic devices used in the optical industry, such as band gap filters, laser mirrors, or fiber Bragg gratings. The interaction of these structural filters with wavelengths of light between 475 nm and 520 nm and the animal's visual ecology together suggest that these structures may help improve the detection of pelagic bioluminescence in shallow water at night.

Key Words: invertebrate vision, stomatopod, larvae, photonic structure, bioluminescence

INTRODUCTION

Optical filters are commonly used by animals to modify the spectral or overall sensitivity of their visual systems. Many species of both vertebrates and invertebrates use a reflecting structure (tapetum) behind their photoreceptors to increase photon capture and enhance vision in dim light

[1-4]. Others use coloured filters positioned lateral or distal to their photoreceptors to tune spectral sensitivity by transmitting specific wavelengths of light not absorbed or scattered by the filter [5-7]. We recently discovered an optical structure positioned within the photoreceptive rhabdoms in the eyes of mantis shrimp (stomatopod) larvae from a single family, the Nannosquillidae. These intrarhabdomal structural reflectors (ISRs) are specialized to simultaneously reflect and filter specific wavelengths of light into rhabdomeric tiers above and below the structure, respectively. The ISR appears to be a feature unique to the nannosquillid lineage since all presently examined nannosquillid larvae (six species) test positive for the structures. The ISR is similar to several synthetic devices such as band gap filters, laser mirrors, and (in particular) fiber Bragg gratings used in optical sensors for a wide range of industries. To our knowledge, the mantis shrimp larval ISR is the first example of a naturally occurring analog to these human-made devices.

Specialized optical structures are well known in adult stomatopod eyes [5, 8, 9] that contain visual adaptations such as UV and visible pigment based filters [10, 11], an unsurpassed diversity in colour and polarization sensitivity [5, 10, 12, 13], as well as unique structural reflectors used for visual communication [14]. Stomatopod larvae, by comparison, lack all of these adult features and are understood to have comparatively simple apposition compound eyes. Until this study, the larval stomatopod eye structure has been described as typical of most other planktonic crustacean larvae in the open-ocean habitats (epipelagic and mesopelagic) where they are found. Typical features of stomatopod larval visual ecology include compound eyes with a uniform array of ommatidia and a single photoreceptor type [15, 16]; morphological adaptations for hiding in open-water, such as highly transparent bodies and reflective eye camouflage [17]; and diel vertical migrations, where animals reside at depths during the day and travel to the surface at night, similar to decapod larvae (pers. observ, [18]). Though the daytime depths and migratory behavior of stomatopod larvae have yet to be specifically measured, one study found that collections at 10-200 m daytime depth were sufficient to quantify larval abundance across a geographic region for the species (*Squilla mantis,* [19]).

Compound eyes evolved in crustacean larvae to mediate visually guided behaviors such as predation and anti-predation responses, as well as migration [16, 20]. The gross examination of stomatopod larval eyes from diverse taxa, however, reveals that a single family (Nannosquillidae) deviate from the typical eye structure by their possession of ISRs within the majority of their rhabdoms. In this study we characterize the anatomical and optical properties of nannosquillid larval ISR-containing retinas as well as consider how these structures may influence task specific behaviors in their dim light habitat.

RESULTS

Histology: In general, stomatopod larvae possess a pair of compound eyes composed of several hundred ommatidial units, each using transparent, apposition optics to focus light onto the photoreceptive rhabdom that is similar in structure to other crustacean larvae [21, 22]. The typical crustacean larval rhabdom is formed from a tightly packed column of visual pigment-expressing, inter-digitated microvilli projected from a ring of seven retinular cells (R1-7). Each rhabdom is optically isolated by screening pigments in the retinular cells. In many crustacean larvae, including stomatopods, reflective structures lie on the surface of the retina, between each rhabdom, to camouflage the dark eye in open water [17]. While the majority of stomatopod larval retinas adhere to this typical arrangement, the retinas of nannosquillid speices contain a

conspicuous addition: the ISR. The ISR is a 4-segmented, barrel-shaped structure that sits approximately one-third of the total length from the distal end of the rhabdom (Fig. 1). Electron and light microscopy reveal that distribution of ISR-containing ommatidia is not uniform across the eye but regionalized to the ventral and lateral regions (Fig. 2). A subset of 30-50 ommatidia in the dorsal region of the eye are devoid of ISR structures and instead possess the untiered photoreceptor structure typical of other crustacean larval retinas (Fig. 1F, 2D). Two-photon microscopy further established the three-dimensional distribution of tiered (ISR present) and untiered (ISR absent) ommatidia across the nannosquillid eye (Fig. 2A-B, Movie S1).

Within each ISR is an ordered lattice of spheroid, membranous vesicles, each an average of 153.3 ± 5.6 nm (mean ± 1 standard deviation; Fig S1A) in diameter. TEM and electron tomography reveal that the ordered arrangement of these vesicles is preserved across the membranes of the four primary segments (Fig. 1D) and in three dimensions (Movie S2). Each ISR measures an average of 11.1 ± 1.5 μm long by 4.9 ± 1.1 μm wide and is positioned directly in the optical pathway of light, bisecting the retinular cells (R1-7) of the rhabdom into a proximal (R2, R3, R6, & R7) and distal tier (R1, R4, & R5; Fig. 1). This cellular arrangement is similar to that of the tiered rhabdoms found in the ommatidia of rows one to four of the midband of some adult stomatopod eyes, including adult nannosquillids [12].

Diverse taxonomic sampling of stomatopod larvae for transmission electron microscopy (TEM) or two-photon microscopy revealed that ISRs may only occur in larvae from the family Nannosquillidae. At least four of the 13 genera described in the Nannosquillid family are represented by species in this study: *Pullosquilla thomassini, Pullosquilla litoralis, Alachosquilla vicina, Coronis scolopendra*, and two unknown nannosquillids (1 and 2) currently lacking adult DNA barcode reference sequences but nested within the nannosquillid clade (Fig. 3; Table S1). The absence of ISRs from other stomatopod lineages suggests that this visual adaptation is unique to nannosquillid larval ecology. Additionally, the presence of ISRs in the first and terminal stage larvae suggests that the function serves the animal throughout the entire pelagic phase of life.

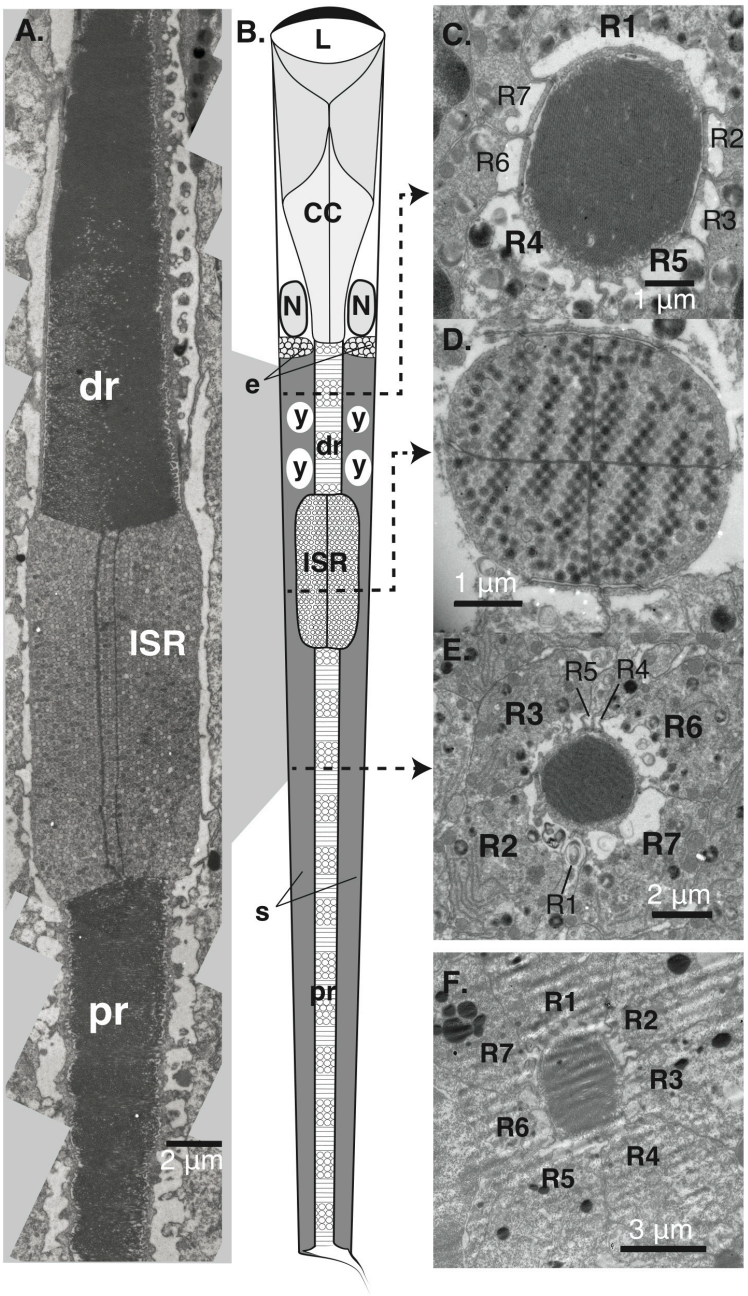

Fig. 1. Anatomy of stomatopod larval ommatidia containing intrarhabdomal structural reflectors (ISR) described by histology. (A) Composite TEM of longitudinal section through a lateral ommatidium. Orthogonal microvilli in the distal (dr) and proximal (pr) rhabdoms flank the ISR. **(B)** Diagram of an ISR-containing ommatidium. **(C)** TEM cross-section through the distal tier of the rhabdom, formed by microvilli from retinular cells R1, R4, and R5 (nomenclature from [10]. Like adult tiered rhabdoms, extensions of the remaining retinular cells are visible and do not contribute microvilli to the rhabdom. **(D)** TEM cross-section through ISR. **(E)** TEM cross-section through the proximal rhabdomeric tier, formed by microvillar projections from retinular cells R2, R3, R6 and R7. **(F)** TEM cross-section through a non-ISR expressing photoreceptor in the dorsal region of the eye. Note the equal contribution of microvilli from retinular cells R1-7. Lens, L; crystalline cone, CC; Retinular cell nucleus, N; reflective eye camouflage, e; yellow long-pass screening pigments [23], y; dark, ommachrome lateral screening pigments, s.

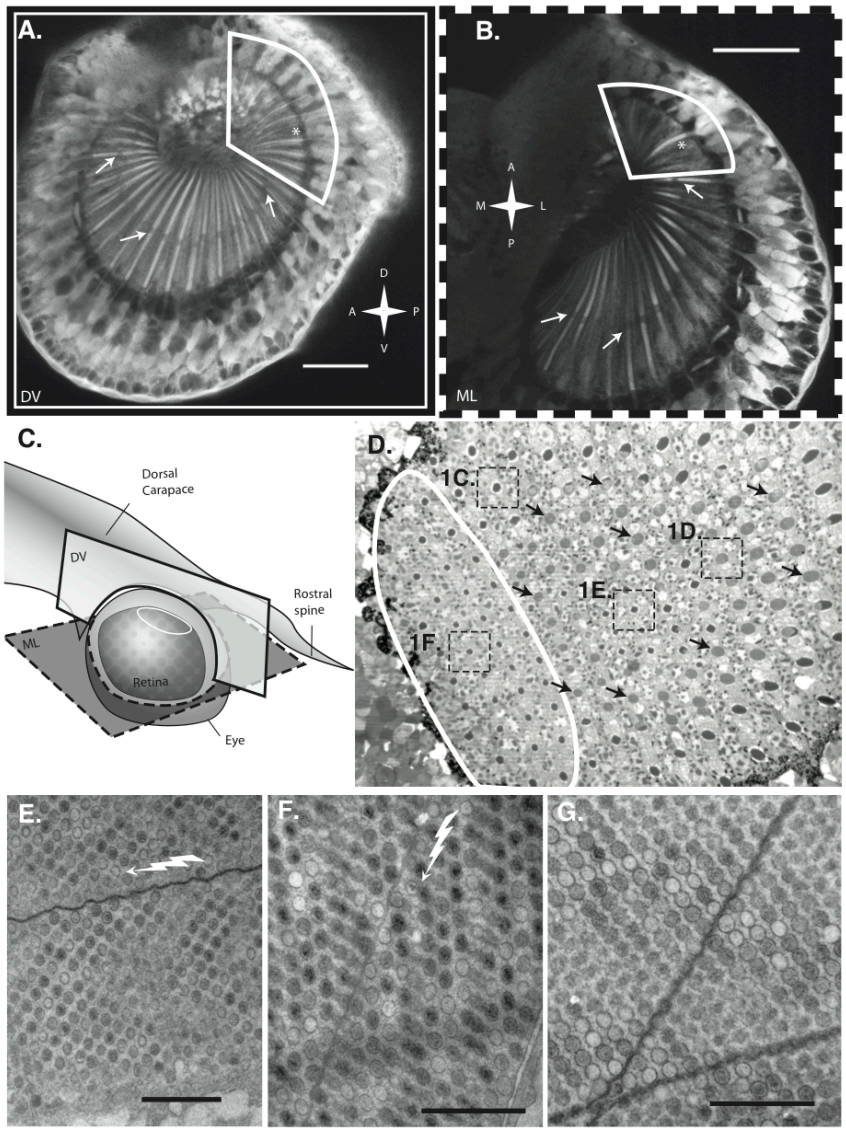

Fig. 2. Regional localization of ISRs across the retina and in the eyes of five different nannosquillid species. (A-B) Two-photon optical sections of *Coronis scolopendra* first stage larval eyes revealing a small region of dorsal pointing ommatidia (within white line) lacking ISR structures (denoted by *). Arrows indicate the dark, less autofluorescent ISRs separating rhabdoms into two distinct tiers. Compasses indicate anatomical directions: A, anterior, P, posterior, M, medial, L, lateral, D, dorsal, V, ventral. Scale bars, 50 μm. **(C)** Diagram of dorsal-ventral (DV) and medial-lateral (ML) sections through eye in A (solid border) and B (dashed border), respectively. **(D)** Light micrograph of retina cross-section from early stage larva, unknown nannosquillid species 1. Boxes depict regions imaged via TEM in Fig. 1C-F. White line denotes dorsal region of untiered ommatidia lacking ISR expression, similar to zone identified in A-C. Arrows highlight subset of ISRs in the remainder of the eye. **(E)** TEM longitudinal section of ISR in last stage larva, *Pullosquilla thomassini* and **(F)** mid stage *Alachosquilla vicina*. Jagged arrows indicate incoming optical axis in longitudinal sections. **(G)** Oblique TEM section of ISR in early stage, *Pullosquilla litoralis* larva. E-G scale bars, 1 μm.

***In vivo* Reflectance Spectroscopy:** The size and arrangement of vesicles within the ISR structures led us to hypothesize that certain wavelengths will be preferentially reflected when the structure is illuminated. To investigate how white light interacts with the ISR, we used a custom microscope system to illuminate, image, and measure reflectance spectra from the pseudopupils of larval ommatidia *in vivo* (Fig. S2). The pseudopupil is the dark spot that moves smoothly across the surface of a compound eye as it rotates, which is produced when the optical axes of a subset of ommatidia align with the optical viewing axis of the observer. Since the ISR lies in the optical axis, we predicted that a distinct reflection profile would be observed when light was imaged axially into ISR-containing rhabdoms.

Prior to this experiment, the phylogenetic distribution of species possessing ISR-containing retinas was not known. Therefore, we tested a diverse range of species available at our field site (Lizard Island, Australia) both to measure the interaction of light with the ISR as well as to examine the distribution of species that express these structures. The experiment was conducted blind to species identity by using wild-captured larvae that were only identified using DNA barcoding after light reflectance measurements were collected [24]. It was observed that some larvae reflect a band of yellow light (average peak of 572 ± 18 nm) from the ventral and lateral ommatidia, but only when illuminated on-axis (Fig. 3; Fig. S2). While side-illumination was sufficient to visualize and measure the blue and green camouflage structures that lie over the pigmented retina [as in 17], only on-axis, epi-illumination could produce a yellow reflectance from the pseudopupil (Movie S3).

DNA barcode identification after the experiment revealed that yellow pseudopupil reflectance was only found in species of the Nannosquillidae family (Fig. 3H). These species represent three of the six species shown to contain ISRs histologically: *Pullosquilla thomassini, Alachosquilla vicina*, and unknown species 1 (Fig. 3H). Stochastic sampling and post-hoc identification precluded reflectance data collection from the remaining species. TEM was used to verify the presence of ISR structures in post-reflectance-measured specimens (Fig. 2D-F), suggesting that ISR structures were the source of observed yellow reflectance. This conclusion was bolstered by coincidence between ISR anatomical regionalization and the pattern of yellow-reflectance observed in only lateral and ventral ommatidia (Fig. 2A-D, Fig 3A-F, Movie S1). Neither yellow reflectances, nor ISR structures were found in the dorsal-most ommatidia.

Of the three nannosquillid species measured for *in vivo* pseudopupil reflectance, different spectral shapes with similar peaks were observed from each species (Fig. S2). Variation in spectral shape and/or reflectivity (seen in Fig S2B-E) may be attributed to subtle differences among species in the material and anatomical assembly of the ISRs (Fig. S1); slight alignment deviations of the sample probe with the optical axis; imaging through multiple layers of dioptrics and rhabdomeric material; and/or different sizes of the eyes and ommatidia aperture among individuals of different species or the same species at different stages. Several ISR reflectances contain short-wavelength components we attribute as contamination from the surrounding, blue-reflective material (eyeshine) that lies on the surface of the retina between ommatidia (Fig S2B, [17]). ISR-containing ommatidia correspond to the lateral and ventral areas of the eye that express this blue eyeshine (Movie S1; Fig. 3A). No contamination arose from the green eyeshine around dorsal ommatidia since these lack ISRs. At present, a pure reflectance from the ISR alone cannot be obtained until methods are devised to adequately remove the crystal from within the center of the eye.

Photonic Modelling: To understand the spectral reflectance from the ISR (Fig. 3G), we developed a semi-analytical optical model. This mathematical model uses a combination of Bragg's law [25] with finite-distance time-domain numerical simulations. By using these methods, we were able to account for the findings of the *in vivo* reflectance experiment and test for any morphological disorder of the ISR potentially induced by TEM. The amount of disorder and the periodicity of the vesicles was determined by calculating the structure factor estimated from TEM micrographs (S.I.). The structure factor of the vesicles within the ISR is related to a face-centered cubic geometry of the vesicles with an estimated lattice constant of 392 ± 7 nm (mean ± 1 standard deviation; Fig. 4A), which takes into account any structural deformations from TEM embedding and slicing of the tissue.

Since the materials contained within the ISR vesicles are not currently known, two different vesicle refractive indices (n_v) were tested in the model: a high-refractive index material, pteridine (n_v 1.70) and a low-refractive index material, lipid (n_v 1.48; further details in S.I.). Pteridine was selected as the high-refractive index material due to the similarity in appearance between our TEM results with membrane-bound pteridine granules and those found in other crustacean photonic structures [26-28]. Our model resulted in agreement with the mean experimental reflectivity spectrum for both pteridine and lipid vesicles with a realistic histological expansion factor (ψ) of 5% and 8% respectively (further details in Supplemental Information, Fig S2F, Fig 4B). This is further evidence to suggest that the observed yellow reflectance measured from the larval pseudopupil is produced by the ISR. The residual difference between our predicted and observed reflectivity can be attributed to several factors including potential histological distortion of ISR dimensions (i.e. ψ); unknown dispersion relation for the refractive indices of vesicle and matrix materials; and additional disorder in the orientation and periodicity of the 3D lattice across large volumes outside the range of TEM tomography (Fig S2F-J).

Though we were able to collect sufficient data to describe the reflection properties of the ISR, we were unable to measure how light is transmitted through the structure. The location of the ISR within the rhabdom poses a logistical problem for collecting light transmission data. Frozen, fresh, or fixed sectioning methods all distort the vesicle lattice, affecting spectral transmission. Though transmission data could not be collected, gross dissection and visual inspection of fixed retinas revealed that ISR structures lack colorful pigments (Movie S4) suggesting that any transmitted wavelengths are likely the difference between the incident light and the reflection or any scattering from the photonic structure, rather than absorption by photostable pigments.

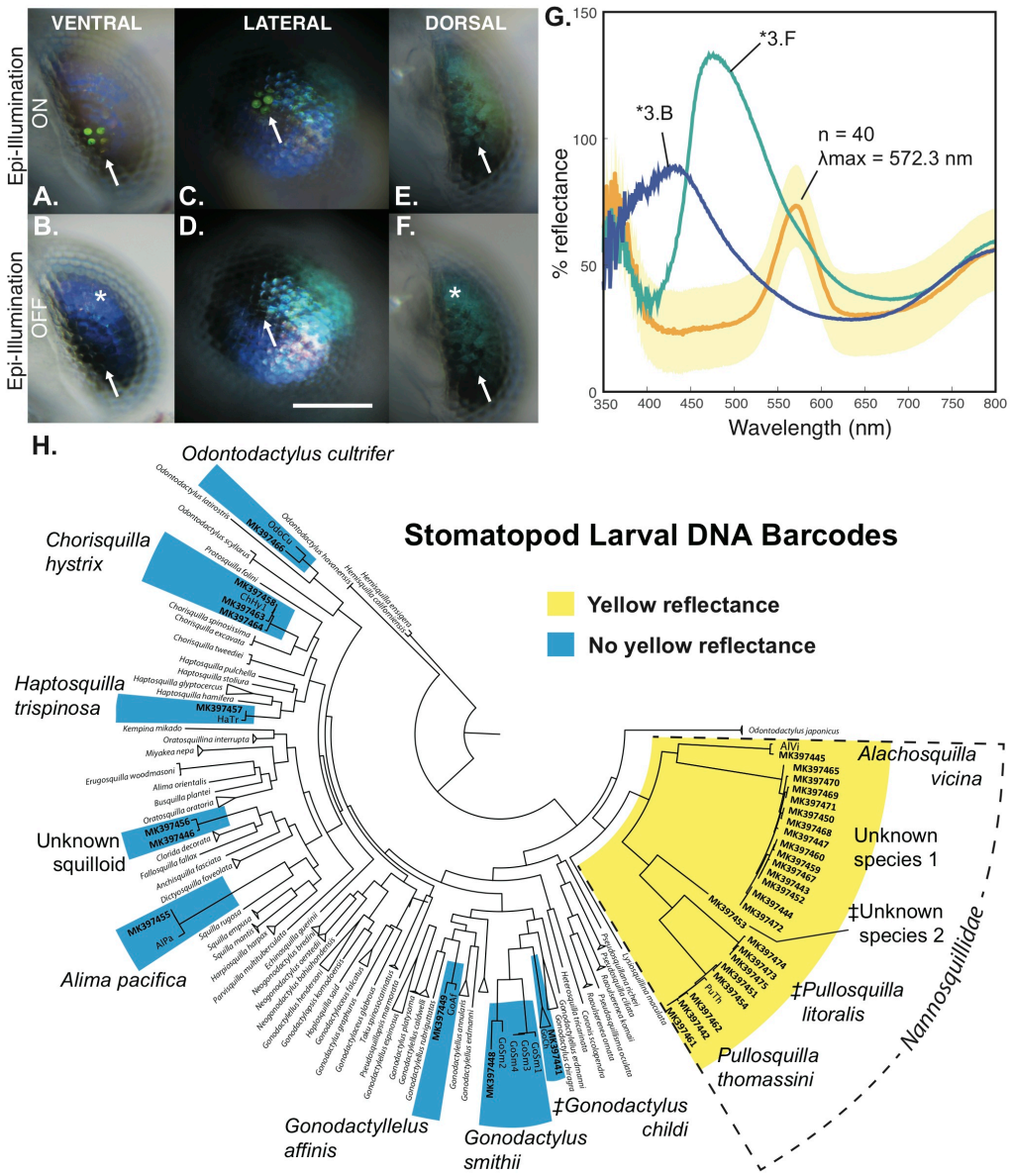

Fig. 3 ***In vivo*** **illumination of the larval eye pseudopupil with on-axis incident light reveals a sharp, yellow reflectance from ISR-containing ommatidia in nannosquillid species only. (A-F)** Illumination of a single nannosquillid eye (Unknown species 1) oriented in three different directions with on-axis (epi) incident illumination on and off. The only condition varied between each pair of ventral, lateral, or dorsal images is the state of the epi-illuminated light (on or off; as in Movie S3). White arrows indicate pseudopupil. Side-illumination was not used during spectral measurements. Scale bar = 150 μm for all images. **(G)** Yellow line, mean reflectance spectra of axially illuminated pseudopupil measurements from 40 individuals of Unknown species 1 (plotted in Fig S2B). Yellow shading, standard deviation of all reflectance spectra used to calculate mean pseudopupil reflectance. Blue and green lines, mean eye camouflage reflectances from regions denoted by * in B (n=4) and F (n=2). Mean blue and green reflectances were measured from the individual photographed in A-F. **(H)** Maximum likelihood tree of cytochrome oxidase I DNA barcodes from adult references and larval sequences. Sequences highlighted in yellow indicate larvae in which a yellow pseudopupil reflectance was measured. Sequences highlighted in blue represent larval eyes that did not produce yellow reflectances in epi-illumination experiment. ‡ indicate barcoded species where reflectance was not measured, but ISR absence or presence was determined by histology only.

DISCUSSION

The discovery of ISR structures raises three major questions. First, what source of light in the nannosquillid larval habitat interacts with the ISRs? Stomatopod larvae encounter few sources of light in this range of the visible spectrum since, like many other larval crustaceans, they live in dim, blue water by day (10-200 m depth) and come to surface only at night (1 m depth). Though the broad irradiance spectrum of moonlight is brighter during periods around the full moon, nannosquillid larvae only rise to the surface between the new and the quarter phases of the moon (pers. observ; pers comm. RL Caldwell) when the total irradiance is 1/100 to a 1/10 that of full moonlight [29]. Furthermore, since moon rise occurs 30 and 60 minutes later each day, the moon may not rise for large portions of a given night when it is full. The only other source of long-wavelength light in this dim-light habitat is bioluminescence (BL). BL has evolved multiple times in diverse pelagic taxa, resulting in a range of peak emission wavelengths that vary with depth. The majority of bioluminescent species live in the deep-sea and emit narrow spectra that peak between 460 nm and 500 nm [30]. And while there are less than half as many bioluminescent species characterized from shallow water (where mantis shrimp larvae reside), the emission spectra of these species are red-shifted, with peaks between 475 nm and 520 nm [30]. Such emission spectra often contain more long-wavelength radiation than the surrounding space light, which may provide a salient signal in the close range of nannosquillid larvae, which measure 2 - 12 mm in body length.

In such a visual environment, could the ISR even improve contrast detection of BL? One known mechanism for improving BL contrast detection is the use of yellow, transmissive filters in the lenses of many deep-sea animals. In these species, a greater proportion of the longer wavelengths of BL emission spectra are able to reach photoreceptors, which is proposed to improve the contrast of a BL target against the shorter-wavelength dominant background of the deep sea (for example [31, 32]). The ISR does not, however, operate in the same way as it is not a short-wavelength absorbing, long-pass filter. Rather, it is a long-wavelength reflector that also removes a narrow band of wavelengths from being incident on the proximal tier of photoreceptors. Since many of the variables surrounding nannosquillid ecology and visual physiology have yet to be described, we developed a visual model to assess the potential function of the ISR. This model tests the minimal possible effect of ISRs on nannosquillid sensitivity when viewing BL light sources of different peak wavelengths. The model estimates the relative proportion of photons captured (quantal catch, QC) by the two rhabdomeric tiers from an incoming light source both with and without the 50% reflective and filtering effect of the ISR (full details in Supplementary Materials, [based on 33]). Different combinations of the two known nannosquillid visual pigments were used in each tier of the rhabdom (450 nm and 500 nm lambda max, Fig. S3A; [15]).

All visual pigment scenarios of the model predict an increase in QC in the proximal tier, with the maximum increase of 11% occurring when the visual pigment lambda max (λ_{max}) is 500 nm. Moreover, this maximum gain in photon capture occurs when the BL emissions peak is between 475 nm and 520 nm, matching the range of BL in the shallow pelagic habitat (Fig 4; [30]). The proximal tier also receives a decrease in QC, regardless of visual pigment expression. The most interesting scenario occurs when the distal and proximal tiers have a λ_{max} of 500 nm and 450 nm respectively as the ISR acts to enhance the difference between the number of photons absorbed by each tier (Fig 4F). Opponent processing of this amplified difference between tier outputs would create a novel mechanism for increasing the contrast of any such

shallow water BL against the background. Overall, these calculations demonstrate that the ISR has the potential to alter the relative photoreceptor absorbance by simultaneously reflecting a narrow waveband of light and filtering specific wavelengths from the transmitted component. To experimentally test this hypothesis, future research must characterize the transmission of the ISR, the chemical nature of the ISR materials and the optical properties of the overlying structures (lens & crystalline cone), as well as assess the spectral sensitivity of each rhabdomeric tier in a nannosquillid retina, and radiometrically quantify the larval light environment.

Finally, which ecological pressures might have led ISRs to become localized in specific regions of the eye? In the lateral and ventral regions of the eye, ISRs would be beneficial for imaging point sources of bioluminescent light horizontally and below [22] the animal. The ISR may have evolved in those positions in the eye as a selective advantage for gaining more visual information about a specific food resources and aiding predation. For these animals, the dorsal regions of their eye are unlikely to be involved in targeting food and therefore correlating with the lack of the ISRs. In comparison to other species of stomatopod larvae, nannosquillid larvae are much smaller and faster swimmers (pers. observations). Future evaluation of nannosquillid larval behaviour may reveal that they use different predation strategies relative to other, often sympatric species of mantis shrimp larvae.

Stomatopods, at all life history stages, continue to provide a compelling system for understanding visual adaptation in the ocean. We have described a new type of visual structure that functions concurrently as both a transmissive and reflective colour filter in stomatopod larval eyes. Looking forward, the homology between these ventral and lateral larval nannosquillid ISR ommatidia and tiered adult stomatopod rhabdoms may provide insight into the developmental mechanisms that led to the rise of the elaborate colour vision system found in many adult stomatopod eyes and the evolution and development structural optics in animals.

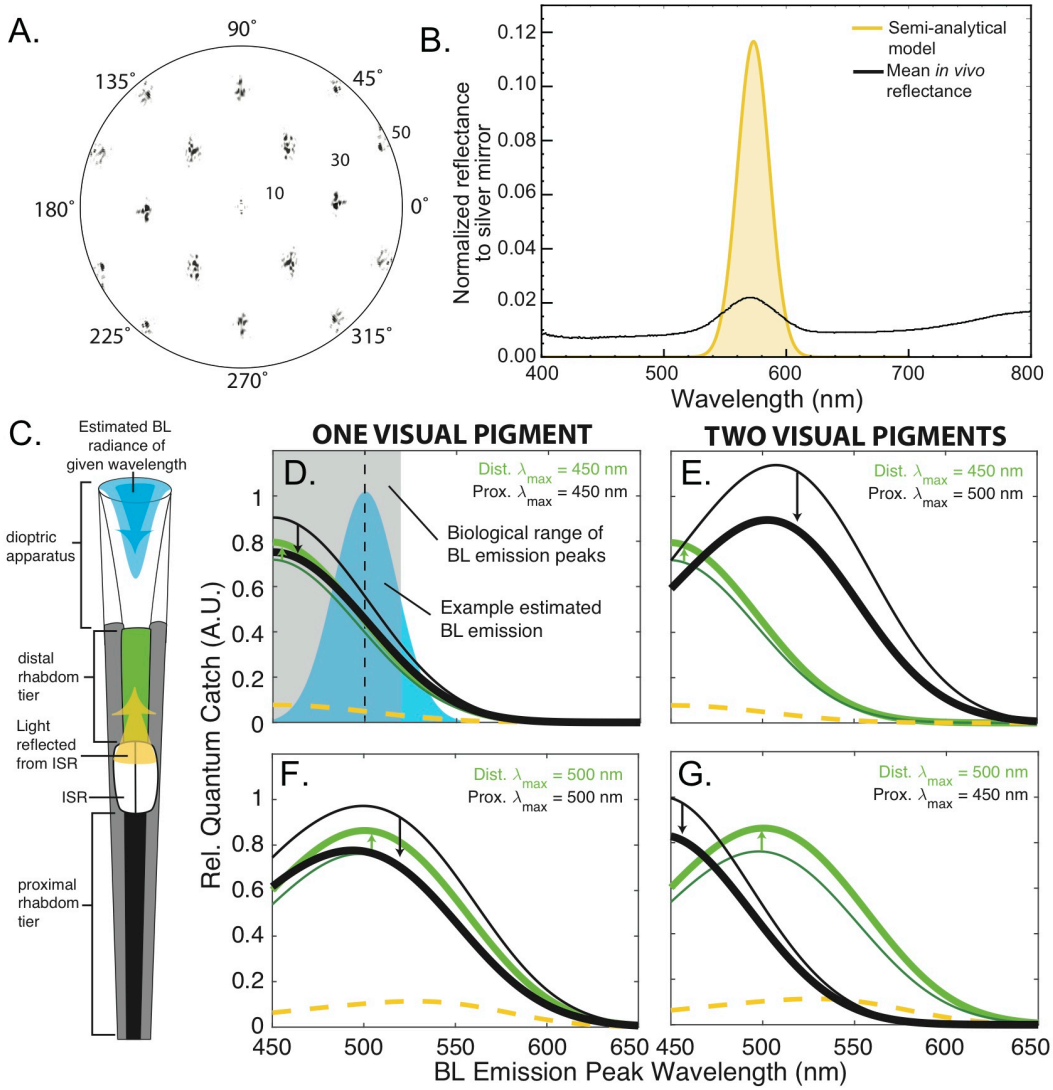

Fig. 4. Results of two optical models (A) Two-dimensional structure factor unveiling the FCC packing of the vesicles in the ISR, measured from TEMs of unknown nannosquillid 1 retina. **(B)** Comparison between the optical response of the ISR predicted by our semi-analytical model for lipidic vesicles and the experimental data, yellow and black curve, respectively. The model indicates an exact correspondence between the predicted wavelength of maximum reflection and the observed wavelength-selective response. Both calculated and measured mean spectral reflectance were mathematically normalized to a silver mirror. **(C)** Diagram representing different components of QC model to BL light sources modeled with and without experimental ISR reflectance. Colors correspond to traces in D-G **(D-G)** Relative proportion of photons captured from different BL wavelength emission spectra. Calculations for distal and proximal tier contain different combinations of visual pigments with peak absorbances (λ_{max}) of 450 nm and 500 nm (combinations indicated top right of each panel). Left two panels (D & F) contain one visual pigment; Right two panels (E & G) contain two different visual pigments. Green traces, QC calculated for distal (Dist.) tier rhabdom; black traces, QC calculated for proximal (Prox.) tier rhabdom. Thin line, QC calculated for ommatidium without ISR; thick line, QC calculated for ommatidium with ISR; yellow dashed line, amount of light reflected from ISR that is absorbed by the receptor. Example BL emission spectrum with peak emission at 500 nm in blue; intersection of black dashed line with green curves represents QC calculated to the 500 nm peaking BL spectrum. Grey shading denotes range of biologically relevant estimated BL emission spectra in the shallow pelagic environment reviewed in [30].

ACKNOWLEDGEMENTS

General: We would like to thank the following people for help with this work: Animal collection and identification: Megan L. Porter, Roy L. Caldwell, Elliott P. Steele, Sitara Palecanda, Jenny Gumm, Lindsdey DeMelo, the Marine Resources Center at the Marine Biological Laboratory, and Australian Museum Lizard Island Research Station, run by Lyle Vale and Anne Hoggart; Spectral measurements and analysis: Tom Jordan, Justin Marshall, John Cataldi, Sonke Johnsen, Simon Lauchlan; Manuscript feedback: Paloma Gonzalez-Bellido, Alice Chiou, Camilla Sharkey, Rachael Feord, Jenny Gumm.

Funding: US Air Force Office of Scientific Research (FA8655-12-2112 and FA9550-12-1-0321) and a travel grant from the Australian Microscopy and Microanalysis Research Facility Travel and Access Program (2010).

Author contributions: KDF made the initial discovery and performed experiments. KDF, TWC, NWR designed the experiments and analyzed the data and wrote and edited the manuscript. TEM by KDF and JM; photonic modelling by GJ & SV; BL modeling by DW; and 2-photon microscopy prep by KDF and imaging by TJW. Figures created by KDF with additions by DW, GJ, and revisions by co-authors.

Competing interests: Authors declare there are no competing interests.

SUPPLEMENTAL MATERIALS

Materials and Methods

Animals & DNA Barcode Identification: All animals were captured at night while wading in shallow water (1-2 m depth) with dip nets and underwater lights at Lizard Island Research Station (August 2015; Queensland, Australia). Stomatopod larvae were sorted from the total plankton catch and stored in cups of seawater until completion of in vivo measurements. Identification was accomplished using previously published methods for DNA barcoding [24]. In brief, telson tissue was fixed in absolute ethanol and transported to the University of Bristol where total DNA was isolated (DNA XS, Machery-Nagel) and DNA amplicons of the cytochrome oxidase 1 mitochondrial gene were generated. Amplicons were sequenced (Eurofins Genomics, UK) and aligned to a database of manually curated stomatopod reference sequences (Geneious Pro 5.5.6) to generate a maximum likelihood phylogenetic tree (PHYML, [34]). Positive identification of a sample to a reference was given if the sequences exhibited either reciprocal monophyly or less than 3% sequence divergence. Several larval specimens were able to be identified to family (Nannosquilidae) due to their nesting within references of this taxonomic unit. These species were thus referred to as “unknown species 1” and “unknown species 2” since a reference barcode does not currently exist to the species level for this group of samples (Fig 3H). These two different species of Unknown nannosquillid represent one that is unique to this study and one that corresponds to a nannosquillid larval species found in a previous study of larval photoreceptors (KM982429, [15]). The same assignments were also

done for two larval sequences nested within the Squilloid superfamily, referred to as "unknown squllioids." A complete list of sample sequences and their Genbank accession numbers is provided in Supplemental Table S1. One sequenced larval species, *Pullosquillia litoralis*, lacks a published adult reference CO1 sequence and was identified via direct collection from hatched clutches collected at the University of California Berkeley Gump Station (Moorea, French Polynesia). *Coronis scolopendra* larvae were hatched from morphologically identified and isolated adults, therefore they did not necessitate the use of DNA barcoding methods for identification.

***In vivo* Reflectance Measurements:** In the field, a Leitz Dialux 22 compound microscope (Wetzlar, Germany) was modified to fit two custom machined optical fiber adaptors that were mounted in place of the eye pieces. An optical fiber (1000 um UV-Vis, Ocean Optics) was attached to each adaptor and connected to either a white light source (tungsten LS-1, Ocean Optics) or a spectrometer (QE6500, Ocean Optics) connected to a computer (MacBook Pro, Apple) running SpectraSuite software (Ocean Optics). The z-plane of each optical fiber adaptor was adjustable so that the focal point of each optical fiber could be fixed through the objective. This was accomplished by connecting the light source to one adaptor and focusing the beam onto a white standard while looking down the eye piece, then doing the same procedure in the reverse position for the second optical fiber adaptor. Once both optical fibers were focused, all imaging took place through the digital camera mount (Canon D-series). Live larvae were fixed to sticks with cyanoacrylate adhesive and mounted in a calibrated angle holder. The mounted larva was then immersed in a tray of seawater and imaged via a submerged 10× microscope objective (Carl Zeiss 4820813, West Germany) protected with clear plastic film (Fig. S2A). A goose-neck laboratory lamp was used to illuminate the specimen from the side for focusing purposes but was turned off for all spectral measurements. A Spectralon diffuse white standard (Labsphere; North Sutton, NH, USA) was affixed near the larva to generate a reference reflectance measurement from the epi-illumination light source through the microscope. Dark (0% reflectance) measurements were collected by shunting the light to the camera viewing mount. In this way, all internal reflections through the microscope system were removed from the reflectance measurement. Once dark and white standards were generated, the pseudopupil of the larval compound eye was brought into focus and spectral reflectances recorded. Off-optical axis, epi-illumination measurements of regions of the eye outside the pseudopupil produced similar reflectance spectra from the eye camouflage as were previously recorded using 45˚ side-illumination [17], though reflectivity was greater in the epi-illumination system than when measured using side-illumination (i.e. Fig. 3G vs. [17]). Epi-illuminated reflectances of the pseudopupil often contained contributions from the off-axis reflective camouflage due to the size of the illumination spot and reflectance sample area exceeding the size of the pseudopupil, which contained four to six ommatidia. On-axis pseudopupil and off-axis reflectance measurements were collected from the ventral, lateral and dorsal region of each eye. Photographs were also collected of each specimen in on- and off-illumination conditions by setting a partial shunt between the camera and the eyepiece connected to the light source (Fig. 3; Movie S3). Spectra were plotted and analysed using Matlab2015b to generate total ISR reflectance averages as well as an average pseudopupil reflectances from each ISR-expressing species measured (Fig. S2B-E)

Electron & Two-Photon Microscopy: Eyes were dissected from live animals in the field immediately post reflectance measurements and fixed with 2.5% glutaraldehyde in PEMS buffer

[0.05 M PIPES, 0.05 M PIPES 2K, 10 mM EGTA, 0.5 mM $MgCl_2$, and 3.8% sucrose, pH 7.0; based on [35] for 60 min with intermediate gentle agitation. Remaining tissue was fixed in absolute ethanol for DNA barcoding identification. Eye tissue was then washed 3 x 10 min in PEMS buffer and stored in fresh buffer at 4˚C for transport to University of Maryland Baltimore County (UMBC) Porter Imaging Facility or University of Bristol Wolfson Imaging Facility. The remaining body tissue was fixed in absolute ethanol for DNA barcoding for identification post hoc. Eyes were postfixed for 60 min in 1.0% osmium tetroxide in water, washed 3 x 10 min in megapure water, then gently agitated in a second postfix of 2% uranyl acetate aqueous solution for 60 min. Samples were dehydrated in an ethanol series before being transferred to propylene oxide for slow infiltration with Epon resin (Taab). Each infiltration step occurred for a minimum of three hours followed by a final embedding in 100% resin overnight. Tissue was then transferred to fresh resin and polymerized 7-8 hours at 70 ˚C. Ultrathin sections (70-80 nm thickness) were cut using a diamond knife, and imaged via a Zeiss 10 CA transmission electron microscope at 60 kV (UMBC) or a FEI Tecnai 12 120kV TEM (Bristol).

TEM micrographs were analysed using ImageJ Fiji software [36] to measure dimensions of ISR structures, vesicles, and rhabdoms. Since veiscles were often observed as ellipsoid in TEM micrographs, the average diameter (d) of each ISR vesicle was determined by measuring the area (A) of an ellipse drawn along the membrane of the the two-dimensional image of each vesicle and using the equation

$$d = 2\sqrt{\frac{A}{\pi}}.$$

Two unknown nannosquillid species 1 specimens were used for conducting TEM tomography experiment (LI15001 and LI15008). Serial sections of 300 nm thickness, were cut from Epon embedded tissue and mounted on open-slot copper grids coated with Formvar film. Prior to visualization, 15 nm gold fiducials (Aurion, NL) were applied to each side of the grid. The sample was then mounted in a Fischione tomography sample holder and the images recorded on an FEI 4k x 4k Eagle camera using FEI Tomography acquisition software in an FEI Tecnai 20, fitted with a LaB6 filament and operated at 200kV. Tilt series were then reconstructed using IMOD software (Boulder , Colorado) and segmented using AMIRA software (FEI Visualization Sciences Group, Bordeaux).

An individual from unknown nannosquillid species 1 (LI15030) and a first stage *Coronis scolopendra* larva hatched from captive adults in the laboratory (Marine Biological Laboratory, Woods Hole, MA) were fixed, dehydrated, and cleared for two-photon microscopy using previously published methods [37]. Imaging of eye structures was completed using an Olympus XLSLPLN25XGMP objective, exciting autofluorescence using a Newport Spectra-Physics InSight® DS+™ laser at 810 nm, and generating average images (from 32 frames) with a resonant scanner as part of a Bruker (Prairie Technologies) Ultima IV *In Vivo* Microscope using GFP and RFP detection channels. The voxel resolution was 0.2 μm in X, Y and Z. Images were compiled and animated using Vaa3D [38] and Fiji software.

Photonic Model: To understand the origin of the wavelength-selective response observed from the pseudopupil we developed a semi-analytical model. Our model combines an analytical

approach (Bragg's law [25], and numerical simulations (Finite distance time domain, FDTD) to describe the optical properties of the ISR.

First, to estimate the structural parameters of the ISR we measured its structure factor starting from TEM images. All TEM and reflectance data used in the model are from unknown nannosquillid species 1, which provided the most complete set of data. The structure factor (S(q)) is formally defined as

$$S(q) = \frac{1}{N}\langle \sum_{i,j=1}^{N} e^{-iq\bullet(r_i - r_j)} \rangle,$$

where q is the wave vector, N the total number of particles, $r_{i,j}$ is the position of the vesicles labeled i and j, and the summation equation $\langle ... \rangle$ denotes ensemble average. The structure factor allowed us to quantify the positional disorder of the ISR (Fig. 4A). From the structural factor we then integrated S(q) along the direction connecting to vesicles to estimated the lattice constant (α), which was determined to be 392 ±7 nm.

Our analytical approach used Bragg's law to predict wavelength position (λ) of the optical response of the periodic crystal to incident light

$$\lambda = a' * n_{eff},$$

where n_{eff} is the effective refractive index, defined by $n_{eff} = \sqrt{\phi * {n_v}^2 + (1-\phi) * {n_m}^2}$ with the refractive index of the vesicles (n_v) and the refractive index of the surrounding matrix (n_m). The constant ϕ is the filling fraction of the FCC crystal (i.e. the fraction of the crystal structure occupied by the vesicles) which is defined as $\phi = \frac{\frac{16}{3}\pi * (r')^3}{(a')^3}$. The variables a and r are the size of the crystal cell and the radius of the vesicles, respectively, adjusted such that $a' = a * \psi$ and $r' = r * \psi$.

It was necessary to consider a range of refractive index values for potential biological materials since the chemical identity of the membrane vesicles or their contents are not presently known. Fig S2G depicts the predicted optical response of the ISR with two different values for vesicle refractive index (n_v), 1.48 and 1.70, which model lipid and pteridine-based systems, respectively. Pteridine was selected as a candidate vesicle material (alternate to lipid) due to its presence in other crustacean photonic systems [26-28]. Changing n_v from 1.48 to 1.70 increases the effective refractive index of the system from 1.35 to 1.39, resulting in both a red-shift of the peak position and an increase in reflectivity. A slight decrease in the shrinkage constant (ψ) from 8% to 5% was applied to offset the red-shift in the higher n_v model so as to align both modeled and experimental reflectance spectra to the same peak for spectral shape comparison (Fig S2G). The variable ψ is a fitting parameter that accounts for artificial compression during the sample preparation for the TEM imaging [39]. In these experiments ψ was equal to 1.08 or 1.05, which translates to an estimation of 8% or 5% compression, or shrinkage, of the tissue, respectively.

Though Bragg's law is powerful tool for analytical analysis of the interaction between light and a material, it is not sufficient for determining intensity or spectral width of the reflection. For this reason we also performed numerical FDTD simulations of the optical response of the ISR using the commercial software LUMERICAL 8.18 (Lumerical 4 Solutions Inc., Vancouver, BC, Canada). These calculations incorporate values of vesicle periodicity (or distribution within the ISR), vesicle size, and the dimensions of the entire ISR structure. Using this approach, we also took into account the finite numerical aperture (NA) of the objective used during the *in vivo* reflectance experiments (NA=0.22), which strongly affects the intensity and width of the response from a periodic system (see Fig. S2H).

To incorporate positional disorder and particle size distribution of vesicles within the ISR structure, we then combined the information generated from the FDTD simulations on predicted reflectance spectral shape with the predicted peak locations determined from Bragg's Law (Fig. S2I-J). To do this, we calculated the peak position for each value of a and r allowed by their distributions, with mean and standard deviation of 392 ± 7 nm and 82 ± 5 nm, respectively. Then, we weighted the numerical line shape with the probability of each value of a and r, such as the value of the associated normalized probability density function. The resulting line shapes (grey lines in Fig. S2I-J) were then fitted with a Gaussian curve that conserves the area of the starting numerical line shape. An unexpected finding in our calculations was that numerical aperture has a larger impact on the calculated optical response than the vesicle size distribution in the structure (Fig. S2H & I). In contrast to this finding, when we account for positional disorder in the calculations, the result is a broader and less intense reflection peak (Fig. S2J).

Experimental reflectance spectra data collected from live larvae (Fig. 3G) used a white diffuser to generate white light reference standards. These experimental data thus needed to be normalized against the total incident radiation (silver mirror) to allow for direct comparison with the theoretical line shape. To do this, we calculated the fraction of light reflected by a white diffuser with a numerical aperture (NA) equivalent to the experimental condition (NA=0.22) using Lambert's Law

$$\mathrm{R}\,(\theta_e) = \frac{\int_0^{\theta_e} cos(\theta) * sin(\theta) d\theta}{\int_0^{90} cos(\theta) * sin(\theta) d\theta}.$$

Where θ_e is the angle of a cone of reflectance off the standard white diffuser, and R (θ_e) is the fraction of light reflected by a standard white diffuser within the defined cone. For a NA of 0.22, θ_e was 9.8˚ and R(θ_e) was 0.03. The experimental data were then multiplied by R(θ_e) to obtain values of reflectance referenced to the total incident radiation.

Even after normalizing the data and accounting for the measured disorder, there was a substantial difference in the intensity between the experimental data and our model (Fig. 3B), which may arise as the result of several possibilities that are not mutually exclusive. First, due to distortion of the tissue during histological preparation, there may be error in the measured size of the ISR itself. Increasing the thickness of the ISR produces an increase in modeled reflectance (Fig. S2G). It may be that *in vivo* the ISRs are much shorter in length than was observed in histological sections, producing a less intense reflection (Fig. S2G).

A second reason for reflectivity differences between the observed and predicted data is related to the true level of disorder in the orientation and periodicity of the 3D lattice of the structure. This information was neither accessible by two-dimensional imagine data, such as TEM, nor the limited thickness able to be sampled using TEM-tomography. Thus, the true values of disorder among the 3D lattice are currently unknown. The third, final reason for differences in the calculated and measured reflectances is that we do not know the true NA of the light returning from the ISR. In the measured reflection, a fraction of the incident light is absorbed into the rhabdom as well as refracted through the animal's light focusing units (crystalline cones and lens). Since our calculations reveal that NA has a substantial impact on the calculated reflectance (Fig S2H), this may be a major source of disparity between observed and predicted spectra.

Quantal Catch Modeling: Mathematical model scripts were compiled in Matlab2017b and are provide as supplemental, annotated documents (visualModelfinal.m; a1SSHtemplate.m). In the visual model, the change in light flux, I, as a function of distance from the start of the rhabdom, z, was calculated by

$$\frac{\mathrm{d}I}{\mathrm{d}z} = -\{\eta(\lambda)f(z)\kappa_v(z)\alpha_v(\lambda) + [1-\eta(\lambda)]\kappa_s(z)\alpha_s(\lambda)\}I(z,\lambda),$$

from Arikawa et al. (1999, [33]). Where η is the fraction of the light flux which is inside the rhabdom boundary as a function of wavelength, λ; f is the fraction of the rhabdom cross-section taken up by a single photoreceptor (in this case $f = 1$); κ_v and κ_s are the peak absorption coefficients of the visual pigment and screening pigments respectively; and $\alpha_v(\lambda)$ and $\alpha_s(\lambda)$ are the normalized absorption spectra. $\alpha_v(\lambda)$ was modelled using a visual pigment absorption template1 [40]. The fraction of light within the rhabdom therefore was approximated by: $\eta(V) = a - b\mathrm{e}^{-cV}$ with a=0.96, b=2.82, c=1.27 and the waveguide parameter, $V = \pi d(n_1^2 - n_2^2)^{1/2}/\lambda$; the rhabdom internal refractive index, n_1=1.36 and the surrounding refractive index n_2=1.34. Further model parameters for distal rhabdom length (34 μm), proximal rhabdom length (72 μm), distal rhabdom diameter (4.5 μm), proximal rhabdom diameter (3.0 μm), and experimental ISR reflectance curve (peak 572 nm) were derived from mean values calculated in this study.

To test the impact of the ISR on light detection, we used a mathematical model of light absorption in rhabdomeric photoreceptors surrounded by screening pigments [33]. Previously, yellow, long-pass lateral screening pigments were described in the distal retinas of nannosquillid larvae (Fig. 1B, [23]). Since the transmission spectrum of these pigments is similar to the reflectance spectrum of the ISR, we incorporated these data into our model of light absorption in the photoreceptors (for transmission spectrum see [23]). The light source used to pass along the photoreceptor in this model was an estimated as a bioluminescent (BL) radiance emission spectrum defined by a Gaussian curve with a full-width at half-maximum of 66 nm (Fig. S3C). This estimated BL was determined by examining the spectral width of common bioluminescent emission spectra in the literature [41, 42]. Since the specific bioluminescent target viewed by nannosquillid retinas is not known, we calculated the quantal catch (QC) for each estimated BL emission spectrum with a peak between 450 nm and 650 nm. Waveguide properties of the rhabdoms are reported in Fig S3D.

The light absorbed by the visual pigment and lateral screening pigments was calculated per unit length of the rhabdom along with the resultant attenuation of the light. Light reaching the ISR was either reflected back along the distal tier, using the normalized experimental reflection spectrum, $R(\lambda)$, calculated for a conservative 50% reflectivity (Fig S3A; Fig. 4) or transmitted through to the proximal tier, with transmission spectrum =1 - $R(\lambda)$, since the absorption spectrum of the IPC was assumed to be nil. The light absorbed by the visual pigment was integrated along the length of the photoreceptor and taken as a measure of relative QC. QC was calculated as a function of the peak wavelength of the target Gaussian light source (each estimated BL). Two visual pigments have been measured from different species of nannosquillid larvae, with peak absorption wavelengths of 450 nm and 500nm [15]. Calculations were thus performed using all potential combinations of opsin templates for these two visual pigments in the proximal and distal rhabdomeric tiers (Fig. S3A).

613 **SUPPLEMENTAL FIGURES, TABLES & MOVIES**

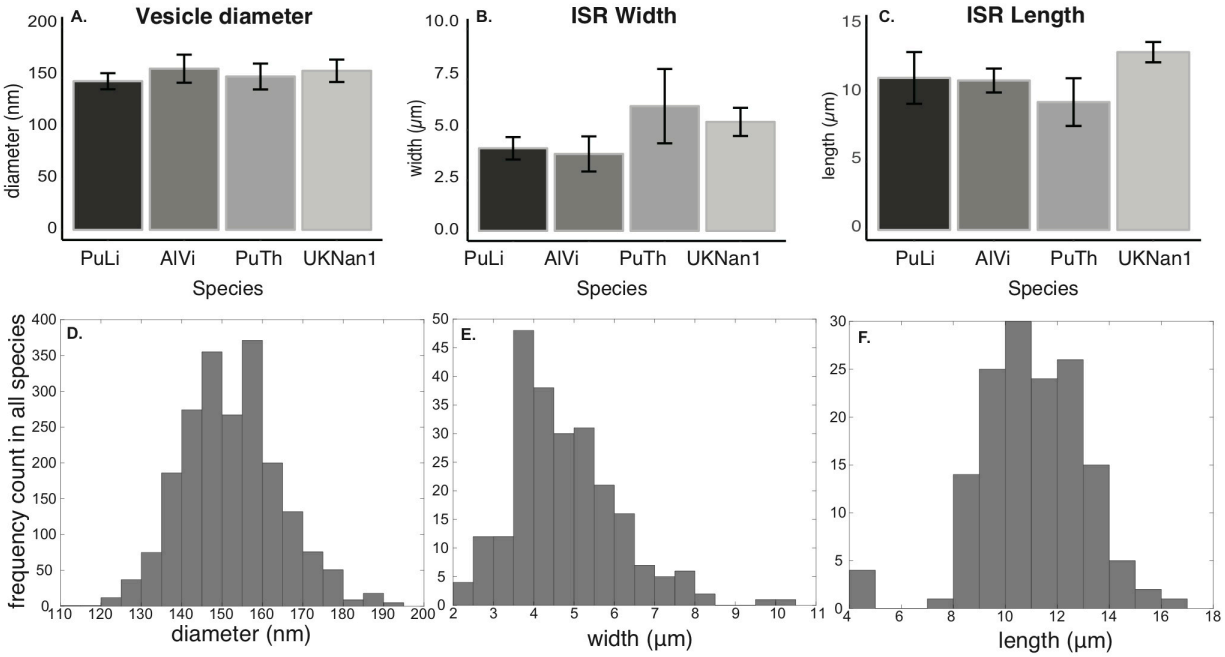

614

615 **Fig. S1. Dimensions of intrarhabdomal photonic structure (ISR) features of different individuals from four**
616 **different species measured from TEM micrographs. (A)** ISR vesicle diameter measurements. The mean vesicle
617 diameters (± standard deviation) are similar between the four individuals of each different species. The overall mean
618 diameter across all individuals is 153.3 ± 5.6 nm (n_{AlVi} = 314; n_{PuLi} = 628; n_{PuTh} = 630; n_{UKNan1} = 498). The number
619 of independent samples precludes any statistical comparison between species. **(B)** The width of ISRs. Mean (±
620 standard deviation) ISR diameters are similar between the four individuals of each different species. The overall
621 mean width of the ISRs is 4.9 ± 1.1 μm (n_{AlVi} = 46; n_{PuLi} = 85; n_{PuTh} = 43; n_{UKNan1} = 60). **(C)** The length of ISRs.
622 Mean (± standard deviation) ISR lengths are also similar between the four individuals of each different species. The
623 overall mean length of the ISRs is 11.1 ± 1.5 μm (n_{AlVi} = 28; n_{PuLi} = 23; n_{PuTh} = 53; n_{UKNan1} = 43). (A-C)
624 Abbraviations for each species, AlVi, *Alachosquilla vicina*; PuLi, *Pullosquilla litoralis*; PuTh, *Pullosquilla*
625 *thomassini*; UKNan1, unknown nannosquillid species 1. **(D-F)** Histograms showing the combined distribution of
626 vesicle diameter, ISR diameter, and ISR length from all species.

627

628

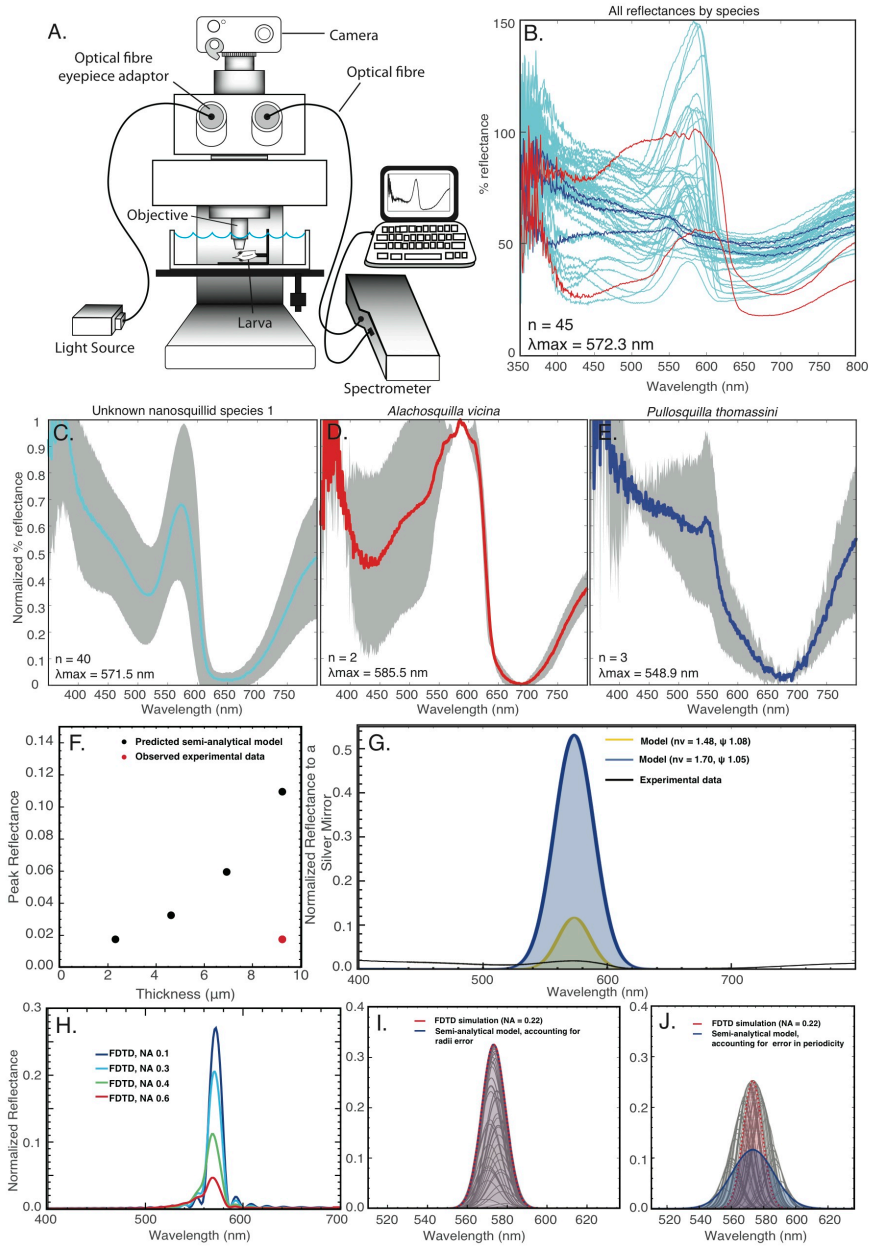

Fig. S2. Measured and modeled light reflected from the ISR (A) diagram of epi-reflectance microscope set-up. Objective has numerical aperture of 0.22, which is relevant to reflectance model in H. **(B)** All reflectances measured from illuminated pseudopupil of nannosquillid larvae. Variation in reflectivity are likely the result of difference in ommatidial size, objective alignment with pseudopupil, contributions from the blue reflective camouflage that surrounds each ommatidium, as well as variables evaluated in F-J. Trace colors correspond to species in in C-E. **(C)** Average pseudopupil reflectance from unknown nannosquillid species 1 **(D)** *Alachosquilla vicina* and **(E)** *Pullosquilla thomassini*. n values and average wavelength of peak reflectance (λ_{max}) reported in the bottom left corner of each figure. **(F)** Peak intensity calculated as a function of the thickness of the ISR. To retrieve a peak reflectance comparable to that of the experimental data it is necessary to reduce the thickness of the ISR. Thus, the difference in observed and predicted thickness may related to distortion of the tissue during histological prepartion. **(G)** Results of modeled reflectance using two different refractive index values (n_v) and associated expansion factors (ψ) versus experimental reflectance (black trace). **(H)** Simulated reflectance as a function of the numerical aperture (NA). Note how reflectivity changes as a function of numerical aperature of the objective used to collect the reflected light. **(I)** Comparison of semi-analytical curves for different values of vescicles' radii **(J)** and ISR periodicity**.**

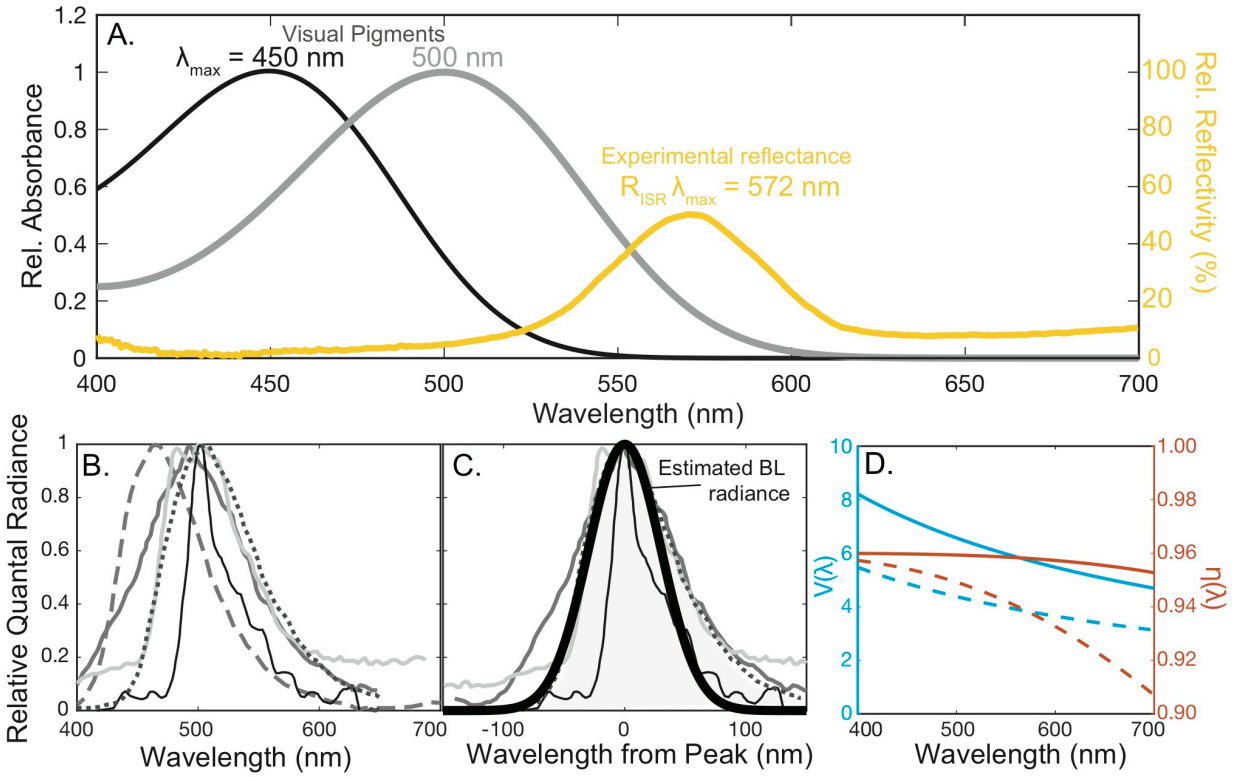

Fig. S3. QC model spectra, waveguide properties, and results calculated using Gaussian model of ISR reflectance. (A) 450 nm and 500 nm peak absorbing opsin templates used to describe two possible visual pigment absorptions in the distal tier. These absorption values were selected based on nannosquillid visual pigment data from the literature [15, 23]. Thin, dark yellow curve, Gaussian model of ISR reflectance used to calculate QC in (E-H). Thick, light yellow curve, average reflectance measurements reported in this paper. Both modeled and measured reflectance calculated for 50% reflectivity **(B)** Sample spectra of bioluminescent sources as a function of wavelength digitized from the literature: dark grey long dash line – Ostracod, *Vargula hilgendorf* [41]; dark grey solid line – Siphonophore, *Bargmannia elongata* [42]; light grey solid line – Midshipman, *Porichythys motatus* [41]; thin black line – Medusa, *Clytia hemisphaericum* [42]; dark grey short dash line – Ctenophore, *mertensiid* [42]. **(C)** The same sample spectra from (B) plotted relative to peak wavelength. Thick black curve shows a 66 nm FWHM Gaussian used in the quantum catch model to approximate different bioluminescent emission spectra. **(D)** The waveguide parameter V (shown in blue), for the distal (solid) and proximal (dashed) rhabdom tiers. For the parameters used here, the rhabdom is multi-mode (V>2.405) for all visible wavelengths. The fraction of light inside the rhabdom, (shown in red) is between 0.9 and 0.96 across the spectrum for both the distal (solid) and proximal (dashed) rhabdom tiers.

Table S1. Larval stomatopod specimens used in TEM, 2-photon, and *in vivo* reflectance experiments. Most larvae were captured from the wild and identified post hoc by DNA barcoding, with the exception of *Coronis scolopendra*, whose larvae were hatched from adults captive in the laboratory. Pseudopupil reflectances were observed in all nannosquillid larvae tested, with the exception of one *P. thomassini* postlarva, likely due to the degeneration of the larval retina after metamorphosis.

Species	**Larval stage**	**Genbank #**	**TEM**	**2Photon**	**Reflectance**
Alima pacifica	last stage	MK397440	x		
Gonodactylellus affinis (Feller & Cronin 2016)	mid stage	KM982428.1	x		
Unknown nannosquillid 2 (Feller & Cronin 2016)	early stage	KM982429			
Gonodactylus childi	early stage	MK397441	x		
Pullosquilla thomassini	last stage	MK397442	x		
Unknown nannosquillid 1	mid stage	MK397443	x		+
Unknown nannosquillid 1	mid stage	MK397444	x		+
Alachosquilla vicina	early stage	MK397445	x		+
Unknown squilloid	early stage	MK397446			-
Unknown nannosquillid 1	mid stage	MK397447			+
Gonodactylus smithii	mid stage	MK397448			-
Gonodactylellus affinis	mid stage	MK397449			-
Unknown nannosquillid 1	early stage	MK397450	x		+
Pullosquilla thomassini	early stage	MK397451			+
Unknown nannosquillid 1	mid stage	MK397452			+
Unknown nannosquillid 2	mid stage	MK397453			+
Pullosquilla thomassini	post larva	MK397454	x		-
Alima pacifica	last stage	MK397455			-
Unknown squilloid	mid stage	MK397456			-

Haptosquilla trispinosa	mid stage	MK397457			-
Chorisquilla hystrix	mid stage	MK397458			-
Unknown nannosquillid 1	mid stage	MK397459			+
Unknown nannosquillid 1	early stage	MK397460			+
Pullosquilla thomassini	last stage	MK397461			+
Pullosquilla thomassini	last stage	MK397462			+
Chorisquilla hystrix	mid stage	MK397463			-
Chorisquilla hystrix	mid stage	MK397464			-
Unknown nannosquillid 1	mid stage	MK397465			+
Odontodactylus cultrifer	mid stage	MK397466			-
Unknown nannosquillid 1	early stage	MK397467		x	+
Unknown nannosquillid 1	mid stage	MK397468			+
Unknown nannosquillid 1	mid stage	MK397469			+
Unknown nannosquillid 1	early stage	MK397470			+
Unknown nannosquillid 1	mid stage	MK397471			+
Unknown nannosquillid 1	early stage	MK397472			+
Pullosquilla litoralis	early stage	MK397473	x		
Pullosquilla litoralis	early stage	MK397474	x		
Pullosquilla litoralis	early stage	MK397475			
Coronis scolopendra	first stage	hatch ID		x	

673

674

Movie S1: Z-stack of the eye of *Coronis scolopendra* first larval stage, measured using two-photon microscopy using autofluorescence of the fixed tissue. ISR structures are visible as slightly darked sections of the rhabdoms, which appear bright. Untiered, non-ISR expressing ommatidia are visible in the dorsal region of the eye.

Movie S2: Three-dimensional arrangement of vesicles (yellow) within the ISRs, segmented from TEM tomography data. This order is preserved across the membranes of the four primary ISR cells (pink). Arrow indicates the direction of incoming, on-axis light.

Movie S3: Yellow reflection is produced from on-axis illumination of ISR containing ommatidia. This video was captured during the *in vivo* reflectance measurement experiments and demonstrates how the pseudopupil moves as the animal rotates the eye in response to changing illuminations under the objective.

Movie S4: Light microscopy of fixed, disassociated retinas reveal that the ISRs do not contain colorful, photostable pigments, which is unlike adult mantis shrimp intrarhabdomal filters. Scale bar, 10 μm.

REFERENCES

1. Loew, E. (1976). Light, and photoreceptor degeneration in the Norway lobster, *Nephrops norvegicus* (L.). Proceedings of the Royal Society of London. Series B.

2. Warrant, E. J., and McIntyre, P. D. (1991). Strategies for retinal design in arthropod eyes of low F-number. Journal of Comparative Physiology A: Neuroethology, Sensory, Neural, and Behavioral Physiology *168*, 499–512.

3. Qiu, X., Vanhoutte, K., Stavenga, D., and Arikawa, K. (2002). Ommatidial heterogeneity in the compound eye of the male small white butterfly, Pieris rapae crucivora. Cell Tissue Res *307*, 371–379.

4. Palmer, B. A., Hirsch, A., Brumfeld, V., Aflalo, E. D., Pinkas, I., Sagi, A., Rosenne, S., Oron, D., Leiserowitz, L., Kronik, L., et al. (2018). Optically functional isoxanthopterin crystals in the mirrored eyes of decapod crustaceans. Proceedings of the National Academy of Sciences of the United States of America *115*, 2299–2304.

5. Cronin, T. W., Bok, M. J., Marshall, N. J., and Caldwell, R. L. (2014). Filtering and polychromatic vision in mantis shrimps: themes in visible and ultraviolet vision. Philosophical Transactions of the Royal Society of London. Series B: Biological Sciences *369*, 20130032–20130032.

6. Stavenga, D. G., and Wilts, B. D. (2014). Oil droplets of bird eyes: microlenses acting as spectral filters. Philosophical Transactions of the Royal Society of London. Series B: Biological Sciences *369*, 20130041–20130041.

7. Arikawa, K., and Stavenga, D. (1997). Random array of colour filters in the eyes of butterflies. Journal of Experimental Biology *200*, 2501–2506.

8. Thoen, H. H., How, M. J., Chiou, T. H., and Marshall, J. (2014). A different form of color vision in mantis Shrimp. Science *343*, 411–413.

9. Marshall, J., Cronin, T., and Kleinlogel, S. (2007). Stomatopod eye structure and function: A review. Arthropod Structure and Development *36*, 420–488.

10. Marshall, N. J., Land, M. F., King, C. A., and Cronin, T. W. (1991). The compound eyes of mantis shrimps (Crustacea, Hoplocarida, Stomatopoda). II. Colour Pigments in the Eyes of Stomatopod Crustaceans: Polychromatic Vision by Serial and Lateral Filtering. Philosophical Transactions of the Royal Society B: Biological Sciences *334*, 57–84.

11. Bok, M. J., Porter, M. L., Place, A. R., and Cronin, T. W. (2014). Biological sunscreens tune polychromatic ultraviolet vision in mantis shrimp. Current Biology *24*, 1636–1642.

12. Marshall, N. J., Land, M. F., King, C., and Cronin, T. W. (1991). The compound eyes of mantis shrimps (Crustacea, Hoplocarida, Stomatopoda). I. Compound Eye Structure: The Detection of Polarized Light. Phil Trans R Soc Lond B *334*, 33–56.

13. Porter, M. L., Bok, M. J., Robinson, P. R., and Cronin, T. (2009). Molecular diversity of visual pigments in Stomatopoda (Crustacea). Visual neuroscience *26*, 255–265.

14. Jordan, T. M., Wilby, D., Chiou, T.-H., Feller, K. D., Caldwell, R. L., Cronin, T. W., and Roberts, N. W. (2016). A shape-anisotropic reflective polarizer in a stomatopod crustacean. Nature Publishing Group, 1–8.

15. Feller, K. D., and Cronin, T. W. (2016). Spectral absorption of visual pigments in stomatopod larval photoreceptors. Journal of Comparative Physiology A: Sensory, Neural, and Behavioral Physiology *202*, 215–223.

16. Cronin, T. W., Bok, M. J., and Lin, C. (2017). Crustacean Larvae—Vision in the Plankton. Integr. Comp. Biol. *57* 1139–1150.

17. Feller, K. D., and Cronin, T. W. (2014). Hiding opaque eyes in transparent organisms: a potential role for larval eyeshine in stomatopod crustaceans. Journal of Experimental Biology *217*, 3263–3273.

18. Cronin, T., and Forward, R. (1986). Vertical migration cycles of crab larvae and their role in larval dispersal. Bulletin of Marine Science *39*, 192–201.

19. Vila, Y., Sobrino, I., and Paz Jiménez, M. (2013). Fishery and life history of spot-tail mantis shrimp, *Squilla mantis* (Crustacea: Stomatopoda), in the Gulf of Cadiz (eastern central Atlantic). Sci. Mar. *77*, 137–148.

20. Cronin, T., and Jinks, R. (2001). Ontogeny of Vision in Marine Crustaceans. American Zoology *41*, 1098–1107.

21. Nilsson, D. (1983). Evolutionary links between apposition and superposition optics in crustacean eyes. Nature *302*, 818–821.

22. Nilsson, D.-E. (1995). Eye design, vision and invisibility in planktonic invertebrates. In Zooplankton: sensory ecology and physiology, P. H. Lenz, D. K. Hartline, J. E. Purcell, and D. L. Macmillan, eds. (Gordon and Breach), pp. 149–162.

23. Jutte, P., Cronin, T., and Caldwell, R. (1998). Photoreception in the planktonic larvae of two species of *Pullosquilla*, a lysiosquilloid stomatopod crustacean. Journal of Experimental Biology *201*, 2481–2487.

24. Feller, K. D., Cronin, T. W., Ahyong, S. T., and Porter, M. L. (2013). Morphological and molecular description of the late-stage larvae of *Alima* Leach, 1817 (Crustacea: Stomatopoda) from Lizard Island, Australia. zootaxa *3722*, 22–32.

25. Bragg, W. L. (1913). The diffraction of short electromagnetic waves by a crystal. *17*, 43–57.

26. Shelton, P., and Gaten, E. (1986). Accessory pigment distribution and migration in the compound eye of *Nephrops norvegicus* (L.)(Crustacea:Decapoda). Journal of Experimental Marine Biology and Ecology *98*, 185–198.

27. Ball, E. E., Kao, L. C., Stone, R. C., and Land, M. F. (1986). Eye structure and optics in the pelagic shrimp *Acetes sibogae* (Decapoda, Natantia, Sergestidae) in relation ot light-dark adaptation and natural history. Phil Trans R Soc Lond B *313*, 251–270.

28. Elofsson, R., and Kauri, T. (1971). The ultrastructure of the chromatophores of *Crangon* and *Pandalus* (Crustacea). J. Ultrastruct. Res. *36*, 263–270.

29. Johnsen, S. (2012). The Optics of Life (Princeton, NJ: Princeton University Press).

30. Widder, E. A. (2010). Bioluminescence in the ocean: origins of biological, chemical, and ecological diversity. Science *328*, 704–708.

31. Muntz, W. R. A. (1976). On yellow lenses in mesopelagic animals. Journal of the Marine Biological Association of the UK *56*, 963–976.

32. Douglas, R. H., Partridge, J. C., and Marshall, N. J. (1998). The eyes of deep-sea fish. I: Lens pigmentation, tapeta and visual pigments. Prog Retin Eye Res *17*, 597–636.

33. Arikawa, K., Scholten, D. G. W., Kinoshita, M., and Stavenga, D. G. (1999). Tuning of Photoreceptor Spectral Sensitivities by Red and Yellow Pigments in the Butterfly Papilio xuthus. Zoological Science *16*, 17–24.

34. Guindon, S., Dufayard, J.-F., Lefort, V., Anisimova, M., Hordijk, W., and Gascuel, O. (2010). New algorithms and methods to estimate maximum-likelihood phylogenies: assessing the performance of PhyML 3.0. Systematic Biol. *59*, 307–321.

35. King, C., and Cronin, T. (1993). Cytoskeleton of retinular cells from the stomatopod, Gonodactylus oerstedii: possible roles in pigment granule migration. Cell Tissue Res *274*, 315–328.

36. Schindelin, J., Arganda-Carreras, I., Frise, E., Kaynig, V., Longair, M., Pietzsch, T., Preibisch, S., Rueden, C., Saalfeld, S., Schmid, B., et al. (2012). Fiji: an open-source platform for biological-image analysis. Nature Methods *9*, 676–682.

37. Gonzalez-Bellido, P. T., and Wardill, T. J. (2012). Labeling and confocal imaging of neurons in thick invertebrate tissue samples. Cold Spring Harb Protoc *2012*, 969–983.

38. Peng, H., Ruan, Z., Long, F., Simpson, J. H., and Myers, E. W. (2010). V3D enables real-time 3D visualization and quantitative analysis of large-scale biological image data sets. Nature biotechnology *28*, 348–353.

39. King, M. V. (1991). Dimensional Changes in Cells and Tissues During Specimen Preparation for the Electron Microscope. Cell Biochemistry and Biophysics *18*, 31–55.

40. Stavenga, D., Smits, R., and Hoenders, B. (1993). Simple exponential functions describing the absorbance bands of visual pigment spectra. Vis. Res. *33*, 1011-1017.

795 41. Widder, E. A., Latz, M. I., and Case, J. F. (1983). Marine Bioluminescence spectra measured with an
796 optical multichannel detection system. The Biological Bulletin *165*, 791–810.

797 42. Haddock, S. H. D., and Case, J. F. (1999). Bioluminescence spectra of shallow and deep-sea
798 gelatinous zooplankton: ctenophores, medusae and siphonophores. Marine Biology *133*, 571–582.

799